Journal of Alloys and Compounds 851 (2021) 156897

Contents lists available at ScienceDirect

Journal of Alloys and Compounds

journal homepage: http://www.elsevier.com/locate/jalcom

Unraveling the nature of Fe-doping mediated inter- and intra-chain interactions in $Ca_3Co_2O_6$

R. Das [a, b], N.T. Dang [c, d, *], V. Kalappattil [a], R.P. Madhogaria [a], D.P. Kozlenko [e], S.E. Kichanov [e], E.V. Lukin [e], A.V. Rutkaukas [e], T.P.T. Nguyen [c, d], L.T.P. Thao [f, g], N.S. Bingham [h], H. Srikanth [a, **], M.H. Phan [a, ***]

[a] Department of Physics, University of South Florida, Tampa, FL, 33620, USA
[b] Faculty of Materials Science and Engineering and Phenikaa Institute for Advanced Study (PIAS), Phenikaa University, Hanoi, 10000, Viet Nam
[c] Institute of Research and Development, Duy Tan University, 550000, Danang, Viet Nam
[d] Faculty of Natural Sciences, Duy Tan University, 550000, Danang, Viet Nam
[e] Frank Laboratory of Neutron Physics, Joint Institute for Nuclear Research, 141980, Dubna, Russia
[f] University of Education, The University of Danang, 550000, Danang, Viet Nam
[g] Department of Physics, University of Sciences, Hue University, 530000, Hue, Viet Nam
[h] Department of Applied Physics, Yale University, New Haven, CT, 06511, USA

ARTICLE INFO

Article history:
Received 15 May 2020
Received in revised form
24 August 2020
Accepted 25 August 2020
Available online 28 August 2020

Keywords:
Multiferroics
Neutron diffraction
Magnetoelectrics
Lowdimensional magnetism

ABSTRACT

The structural and magnetic properties of quasi-one-dimensional (1D) spin-chain compounds $Ca_3Co_{2-x}Fe_xO_6$ (x = 0, 0.1, 0.2 and 0.3) synthesized by a sol-gel method have been systematically studied by means of X-ray diffraction (XRD), X-ray photoelectron spectroscopy (XPS), neutron powder diffraction (NPD), *dc* and *ac* magnetization measurements. The samples adopt a rhombohedral crystal structure with the space group *R-3c* in a temperature range of 5–100 K. Fe ions are found to locate at the trigonal prism Co2 crystallographic sites. Fe doping converts some of low-spin Co^{3+} ions at Co1 octahedral sites into Co^{2+} ions. For the high-temperature paramagnetic phase, the Curie paramagnetic temperature θ_p changes its sign from positive to negative at $x = 0.2$, implying that the dominant magnetic interaction is driven from ferromagnetic (FM) to antiferromagnetic (AFM) upon Fe substitution. A partial low-spin to high-spin state crossover of the Co1 ions is observed at high Fe-doping level $x = 0.3$. All the samples exhibit a long-range spin-density wave (SDW) AFM ordering below T_N, followed by a spin-glass-like transition at T_f. These low-temperature magnetic phases were significantly suppressed upon Fe doping. The Fe substitution in $Ca_3Co_{2-x}Fe_xO_6$ weakened both intrachain and interchain magnetic interactions, caused by enhanced magnetic disorder due to the different magnetic characters of Ising Co and Heisenberg Fe spins.

1. Introduction

Multiferroic materials exhibiting the magnetism-driven ferroelectricity, where ferroelectricity is induced by magnetic ordering, are characterized by a strong magnetoelectric coupling, close ferroelectric transition, and magnetic ordering temperatures [1,2]. It is worth noting that the magnetism-induced ferroelectricity is commonly observed in magnetically frustrated systems, since spin frustration induces spatial variation in magnetization, giving rise to the loss of the lattice inversion symmetry and therefore resulting in the occurrence of ferroelectricity.

Among magnetically and geometrically frustrated materials, the quasi one-dimensional Ising chain compound $Ca_3Co_2O_6$ has attracted intensive attention due to its exotic magnetic properties [3–10]. The rhombohedral *R-3c* crystal structure of $Ca_3Co_2O_6$ contains chains made up of alternating face-sharing $Co1O_6$ octahedra and $Co2O_6$ trigonal prisms along the *c* axis, which are arranged in a triangular lattice in the *ab* plane (Fig. 1). Due to the different crystal electric fields, cobalt ions occupying the Co1 octahedral sites have a

* Corresponding author. Institute of Research and Development and Faculty of Natural Sciences, Duy Tan University, Danang, 550000, Viet Nam.
** Corresponding author.
*** Corresponding author.
E-mail addresses: dangtoan2107@gmail.com (N.T. Dang), sharihar@usf.edu (H. Srikanth), phanm@usf.edu (M.H. Phan).

https://doi.org/10.1016/j.jallcom.2020.156897
0925-8388/

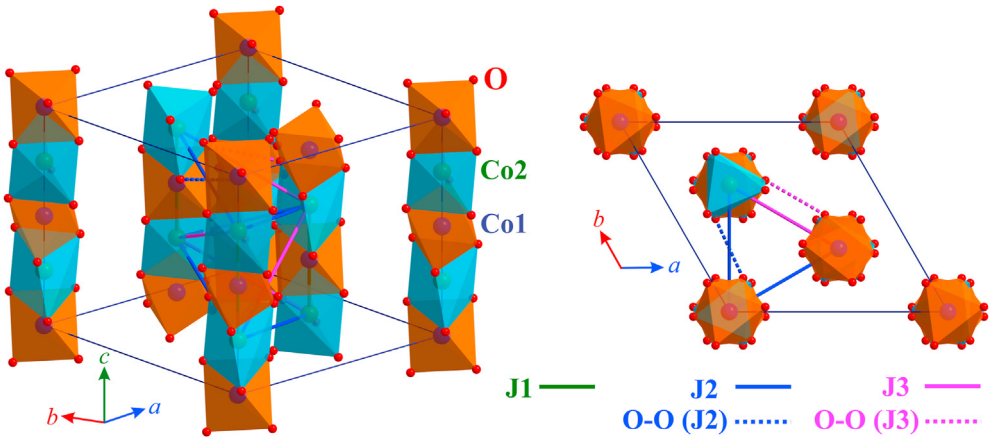

Fig. 1. The crystal structure of $Ca_3Co_2O_6$ at different views. The paths of the intra (J_1) and inter-chain (J_2, J_3) interactions are shown.

low spin state ($S = 0$), while the cobalt ions in the Co2 triangular base prism have a high spin state ($S = 2$) [11]. The intrachain magnetic interaction between Co2 spins (J_1) is strongly ferromagnetic (FM), $J_1 \sim 25$ K, while the interchain magnetic interaction is governed by the weak super-superexchange antiferromagnetic (AFM) interactions J_2 and J_3 through Co—O—O—Co path ways, $J_2 \sim J_3 \approx 1$ K (Fig. 1) [12–14]. The strong difference in strength of the intrachain and interchain magnetic interactions combined with the triangular arrangement of spin chains leads to a geometrical frustration and consequently the complex magnetic behavior with a coexistence of several magnetic states in this system [8,15–19].

It has been reported that $Ca_3Co_2O_6$ exhibits a quasi-1D ferromagnetic ordering inside the chains below 100 K and then a long-range magnetic order below the Néel temperature $T_N = 25$ K [8,15–17]. However, the exact nature of the long-range magnetic order has remained a long-lasting debate. It was initially proposed that the magnetic structure corresponds to a partially disordered antiferromagnetic (PDA) configuration (M, - M, 0), where two third of the ferromagnetic Ising spin chains are coupled antiferromagnetically with each other, while the one third is left disordered with zero net magnetization [20,21]. However, Agrestini et al. have unambiguously shown that the magnetic structure is not a simple PDA state but corresponds to a complex incommensurate amplitude-modulated PDA or the so-called spin density wave (SDW) structure with a wave propagation vector $\boldsymbol{k} = (0, 0, k_z \sim 1.01)$, with a phase shift of 120° between adjacent chains [18,19]. Moreover, the short range magnetic correlations were reported to coexist with the long-range order at low temperature just below the T_N [18,19,22], probably due to the presence of defects in the propagation of the long-range SDW order with stacking faults developed along the c-axis direction [18]. The partial transformation of the SDW state to the long-range metastable commensurate antiferromagnetic (CAFM) state with $\boldsymbol{k} = (0.5, - 0.5, 0)$ was shown to occur at $T_{N2} \sim 10$ K [19]. Notably, the volume fractions of the phases are strongly dependent on the time and the rate of sample cooling [19]. As a result of the delicate competition between these magnetic interactions, an “exotic” spin-glass-like state was found below ~7 K [17,23].

The delicate balance of the intra- and interchain magnetic interactions on the geometrically frustrated triangular lattice makes $Ca_3Co_2O_6$ extremely susceptible to variation in magnetic field, pressure, or chemical doping. Multiple metamagnetic transitions associated with the formation of ferri- and ferromagnetic states, as well as their inter-conversion were observed in $Ca_3Co_2O_6$ upon the application of a magnetic field along the c-axis of the material [15–17]. Notably, we have recently observed a full suppression of the ambient-pressure long-range SDW and short-range phases and a stabilization of the CAFM phase at high pressures $P \geq 2$ GPa [22]. In contrast to the pressure-induced effect [22], the chemical doping has been shown to stabilize the SDW phase and decrease the T_N in $Ca_{2.75}R_{0.25}Co_2O_6$ (R = Dy, Lu) [24] and Fe-doped $Ca_3Co_{2-x}Fe_xO_6$ with $x \leq 0.4$ [25]. The origin of the observed phenomena can be attributed to modifications of the strength ratio between the intra- and interchain magnetic interactions [26]. The calculations have shown that the lower energy magnetic configuration is the CAFM structure for $|J_{2,3}/J_1| < 1.7$ and becomes the SPW structure for $|J_{2,3}/J_1| > 1.7$, where $J_{2,3}$ is the average strength of the interchain magnetic interactions [26]. The pressure-induced stabilization of the CAFM phase has been attributed to the reduction of $|J_{2,3}/J_1|$, due to the more rapid enhancement of the intrachain exchange interactions compared to the interchain ones [22]. In case of the Fe- or R-doped $Ca_3Co_2O_6$ compounds [24,25], the chemical doping reduces the intrachain magnetic interactions and enhances the interchain ones, thus increasing $|J_{2,3}/J_1|$. This consequently stabilizes the SPW phase [24,25,27]. A worthy of note is that while the variation in the magnetic interactions in $Ca_{2.75}R_{0.25}Co_2O_6$ (R = Dy, Lu) was related to the modification in the bond lengths within the exchange pathways [24], it was suggested to arise from the difference in Ising Co and Heisenberg Fe spins in $Ca_3Co_{2-x}Fe_xO_6$ [28]. In the latter case, a low-temperature neutron diffraction study revealed structural modifications in $Ca_3Co_2O_6$ upon Fe doping [29]. However, how such structural changes influence the magnetic properties of the Fe-doped compounds is not fully understood, and there is an open question on how the valence of Co ions evolves with Fe doping.

To shed more light on these, we have performed a systematic study of the structural and magnetic properties of $Ca_3Co_{2-x}Fe_xO_6$ ($x = 0$, 0.1, 0.2, and 0.3) samples by means of X-ray diffraction (XRD), X-ray photoelectron spectroscopy (XPS), neutron powder diffraction (NPD) and magnetometry. Results obtained show that Fe ions locate at the trigonal prism Co2 crystallographic sites. The Fe doping converts some of low-spin Co^{3+} ions at Co1 octahedral sites into Co^{2+} ions. We demonstrate that the Fe substitution weakens both intrachain and interchain magnetic interactions, caused by the enhanced magnetic disorder due to the different magnetic characters of Ising Co and Heisenberg Fe spins.

2. Experiment

Polycrystalline $Ca_3Co_{2-x}Fe_xO_6$ ($x = 0$, 0.1, 0.2, 0.3) samples were prepared by a conventional sol-gel method. Aqueous solutions of

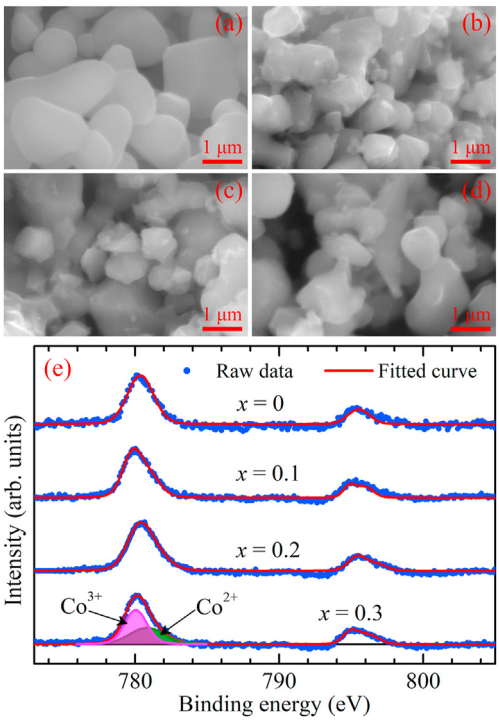

Fig. 2. SEM micrographs of $Ca_3Co_{2-x}Fe_xO_6$ samples with (a) $x = 0$, (b) 0.1, (c) 0.2, and (d) 0.3, and their corresponding XPS spectra at the Co $L_{2,3}$ edge (e).

$Ca(NO_3)_2{\cdot}4H_2O$ (99.0%), $Co(NO_3)_2{\cdot}6H_2O$ (99.999%) and $Fe(NO_3)_3{\cdot}9H_2O$ (99.999%) with stoichiometric ratio of the desired cations and a bridging compound citric acid (99.0%) were prepared and stirred for 30 min to ensure homogeneous mixing of cations. Citric acid was used as a binding ligand to form metal organic complexes. Then the sol was aged at 80 °C in water bath. After aging, the xerogel was dried on a hot plate, to eliminate all of the water. Roughly around 200 °C, auto-combustion occurs, in which a self-sustaining exothermic redox reaction results in a black ashy powder. To improve the crystallinity and obtain the proper phase this ash was calcined at 1000 °C for 1 h.

The structural phase analysis was carried out using a Bruker AXS powder X-ray diffractometer (XRD) with Cu-Kα radiation. X-ray Photoelectron Spectroscopy (XPS) was performed with a PHI VersaProbe II, in ultra-high vacuum (~10^{-8} torr). The neutron powder-diffraction measurements in the temperature range $T = 5$–300 K were performed with the DN-6 diffractometer (IBR-2 pulsed reactor, JINR, Russia) [30]. Diffraction patterns were collected at scattering angle of 90° with resolution $\Delta d/d = 0.025$. The typical data collection time at one temperature was 2 h. The experimental data were analyzed by the Rietveld method using the Fullprof program [31]. Magnetic measurements were performed using a Quantum Design Physical Property Measurement System (PPMS) with the Vibrating Sample Magnetometer (VSM). Magnetization versus applied magnetic field (M vs. H) was measured from $H = 0$–70 kOe for temperatures ranging from $T = 2$–300 K. Using the ac/dc Magnetometry System (ACMS) option of the PPMS, ac susceptibility measurements were performed with frequencies ranging from 10 Hz to 10 kHz at the ac driving field of 5 Oe while warming up from 3 K.

3. Results and discussion

Fig. 2(a–d) shows SEM images of $Ca_3Co_{2-x}Fe_xO_6$ samples with $x = 0$, 0.1, 0.2, and 0.3, respectively. The micrographs indicate that the particles are quasi-spherical in morphology and they are fused together due to high temperature calcination. The calculated average particle size is 300, 240, 225, and 250 nm for $x = 0$, 0.1, 0.2, and 0.3, respectively. A Mössbauer study revealed a pure trivalent valence and high-spin state of Fe ions in $Ca_3Co_{2-x}Fe_xO_6$ [26]. However, the valence evolution of Co ions with Fe doping was unclear. Therefore, in the present study, the XPS data were recorded at the Co $L_{2,3}$ edge and fitted using the CASAXPS software [32] (see Fig. 2e). It should be mentioned that we are unable to resolve the XPS spectra at the Fe edge due to Auger electrons from Co occurring near the Fe L-edge. Additionally, due to the powder nature of the sample and the low (<5 nm) probing depth of the XPS the Co valences should be treated as nominal. From the analysis of the Co 2p XPS spectra, we have found that the undoped sample contains almost Co^{3+} ions, and the Fe substitution converts some amount of Co^{3+} ions into Co^{2+} ones. The fraction of Co^{2+} ions demonstrates an almost linear increase with increasing x from 12% at $x = 0.1$–25% at $x = 0.2$ and then to 42% at $x = 0.3$. The errors in the fits are most likely due to the powder nature of the sample, which leads to enhanced broadening at the absorption edge as well as errors due to potential oxygen vacancies which were not accounted for. Additionally, there are satellite peaks at approximately 790 eV and 804 eV which were not fitted in this present case but, has been shown [33] to be associated with the Co–O charge transfer. Notably, the similar ionic transfer for Co ions was also reported for Pb^{3+}, Sm^{2+} or F-doped $Ca_3Co_2O_6$ systems [34–36]. Moreover, it was established that the Co^{2+} ions prefer to locate at the octahedral Co1 sites and be in the low-spin state [34,35], which is consistent with the magnetization results as shown below.

The crystal structure of the $Ca_3Co_{2-x}Fe_xO_6$ samples has been analyzed by both XRD and NPD. Room-temperature XRD and NPD patterns of the samples are shown in Fig. 3a and b, respectively. The data analysis has revealed that all of the samples are single phase and adopt the *R-3c* rhombohedral crystal structure (see Fig. 3), except for $x = 0.3$, which contains about 4.6 wt % of $CaFeO_3$ impurity (see inset of Fig. 3a). It is worth noting that $CaFeO_3$ has a strong A-type antiferromagnetic order at T_N ~116 K [37–39]. Since no AFM sign of the $CaFeO_3$ was observed from the magnetic measurements (presented below) for the $x = 0.3$ compound, its contribution to the magnetism of the sample can be neglected. It is important to note that as an advantage of the neutron diffraction compared to the X-ray diffraction, NPD allows us to exactly determine the distribution of Co and Fe over their possible crystallographic sites due to the large difference in the neutron scattering lengths of Co (2.49 fm) and Fe (9.45 fm). As a result, we have observed that most Fe ions locate at the trigonal prism Co2 crystallographic sites, consistent with the previously reported works [25,29]. Moreover, the lattice parameters increase with increasing Fe concentration, x, which can be explained due to the larger ionic sizes of high-spin Fe^{3+} (0.645 Å) and low-spin Co^{2+} (0.65 Å) ions compared to those of high-spin (0.61 Å) and low-spin (0.545 Å) Co^{3+} ones [40,41].

In order to understand effects of Fe doping on the magnetic properties of $Ca_3Co_{2-x}Fe_xO_3$, temperature-dependent magnetization was first measured at a magnetic field of 100 Oe with zero-field cooling (ZFC) and field-cooling (FC) regimes, as shown in Fig. 4. At high temperature, the ZFC and FC $M(T)$ curves of all the samples coincide and follow the paramagnetic Curie–Weiss law $\chi = C/(T - \theta_p)$, where θ_p is the paramagnetic Curie temperature and C is the Curie constant (see the insets of Fig. 4). The refined values of C and θ_p, determined by extrapolation of the linear region of these curves, are presented in Table 1. It should be noted that the positive value of θ_p for the undoped sample evidences that FM interactions are dominant in the sample at high temperature. Upon Fe-doping, θ_p decreases monotonously and changes its sign at $x \geq 0.2$ (Fig. 5b),

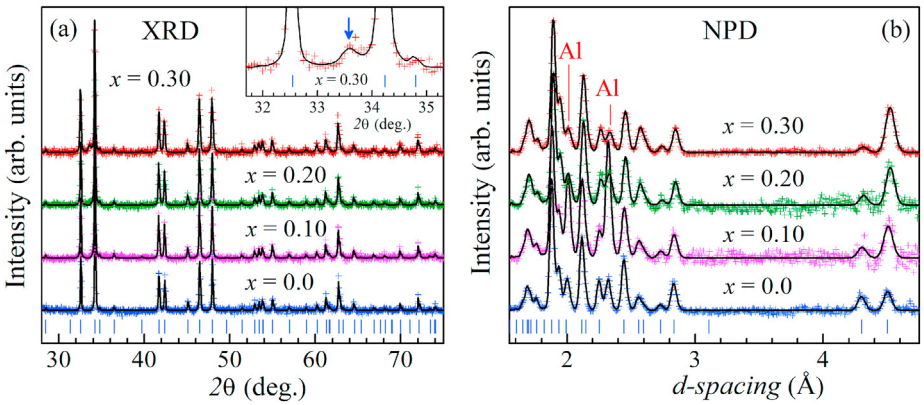

Fig. 3. Room-temperature X-ray (a) and neutron (b) powder diffraction patterns of $Ca_3Co_{2-x}Fe_xO_6$ with $x = 0.0$, 0.1, 0.2 and 0.3, refined by the Rietveld method. The experimental points and calculated profiles are shown. The ticks below represent the calculated positions of the nuclear peaks from the structural phase. The most intense peaks of Al used as a sample cover are marked by symbol Al. The inset in Fig. 3a shows an enlarged view of the region of the diffraction pattern of $x = 0.3$, containing the peak of impurity $CaFeO_3$ marked by an arrow.

lending evidence for the weakened FM interactions and the dominant AFM interactions at higher Fe concentrations. The Fe concentration dependence of the effective magnetic moment, determined by the relation $\mu_{eff} \approx 2.83C^{1/2}$ (μ_B), is shown in Fig. 5. Concerning the Co^{2+} ions, if Fe-doping converts amount of the high-spin Co^{3+} ions at the Co2 sites into Co^{2+} ions, μ_{eff} should decrease in magnitude with increasing x, which is contrary to the experimental result. We recall the above-mentioned assumptions on the preferable location at the Co1 sites and the low-spin state of the Co^{2+} ions. Considering the low-spin state of Co^{2+} ($S = 1/2$) at the Co1 site and the high-spin states of Co^{3+} ($S = 2$) and Fe^{3+} ($S = 5/2$) at the Co2 site, the theoretically calculated spin-only μ_{eff} values have been obtained using an expression $\mu_{eff} = (1 - x)\cdot\mu_{Co2} + x\cdot\mu_{Fe2} + y\cdot\mu_{Co1}$, where $\mu = 2\sqrt{S(S+1)}$, x and y are the fractions of Fe^{3+} and Co^{2+} at their sites, respectively. For $x = 0$, the experimental value of $\mu_{exp} = 5.65$ μ_B is larger than those of the spin-only

Table 1
Characteristic temperatures T_{irr}, T_f and T_N, paramagnetic Curie temperature θ_p, Curie constant C, experimental and theoretical values of μ_{eff} for $Ca_3Co_{2-x}Fe_xO_{3-\delta}$ samples.

x	T_{irr} (K)	T_f (K)	T_N (K)	θ_p (K)	C (emu/mol.Oe)	μ_{eff} (μ_B)
0.0	43.91	8.12	25.10	24.914	3.987	5.645
0.1	10.85	6.54	22.35	15.835	4.1716	5.774
0.2	8.54	5.79	19.38	−3.674	4.756	6.166
0.3	6.38	5.22	17.25	−64.318	6.858	7.404

one of 4.90 μ_B, which can be attributed to the contribution of the orbital magnetic moments of the Co2 ions originated from the spin-orbital coupling and an unusual coordination of the Co^{3+} ions at these sites [27,42–44]. As can be seen in Fig. 5b, the difference $\Delta\mu_{eff}$ between μ_{exp} and μ_{theor} values decreases as x increases to 0.2, indicating the suppression of the orbital moment, which is similar

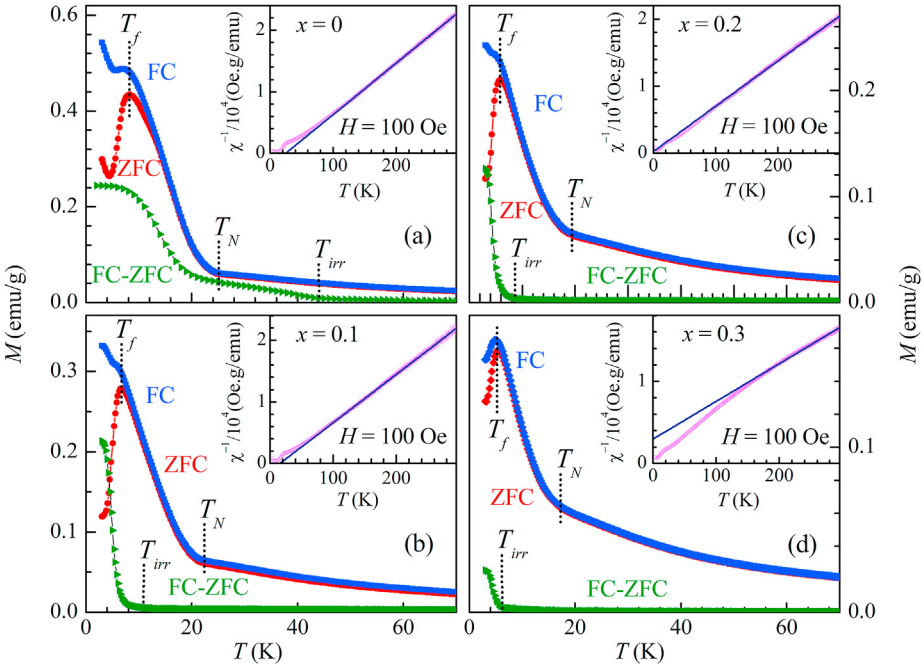

Fig. 4. Temperature dependences of ZFC, FC magnetizations and their difference for $Ca_3Co_{2-x}Fe_xO_6$ with (a) $x = 0.0$, (b) 0.1, (c) 0.2 and (d) 0.3. Insets: Plots of inverse magnetic susceptibility vs temperature for the samples.

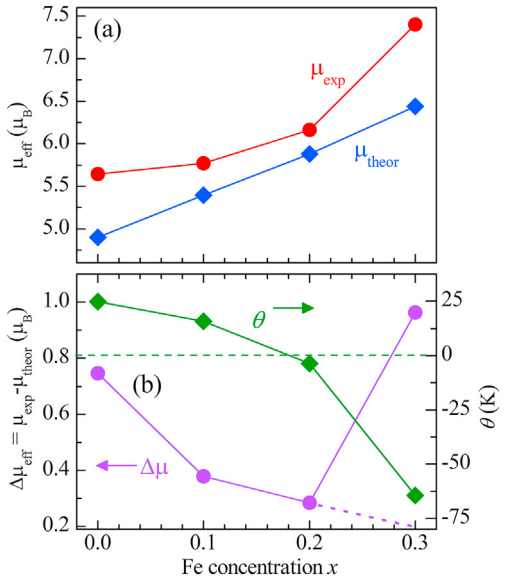

Fig. 5. a) Theoretical and experimental values of μ_{eff} and b) Difference between the experimental and spin-only values of the effective moment (left) and Curie paramagnetic temperature θ_p (right) as functions of Fe-doping concentration.

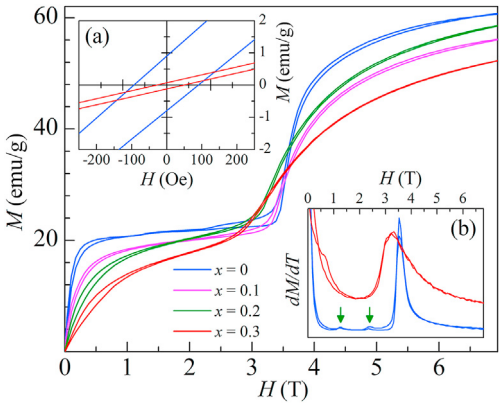

Fig. 7. Magnetic-field dependent magnetization curves of $Ca_3Co_{2-x}Fe_xO_6$ ($x = 0$–0.3) at 10 K. The insets (a) and (b) show an enlarged view around the origin and derivative curves of $M(H)$ at 10 K for $x = 0$ and 0.3.

to that caused by F^- doping [35]. By extrapolating the $\Delta\mu_{eff}$ curve, the orbital contribution is estimated to be ~0.2 μ_B at $x = 0.3$, which is much smaller than the $\Delta\mu_{eff}$ value of 0.96 μ_B obtained for $x = 0.3$ (Fig. 5b). This can be attributed to a partial low-spin to high-spin state transition for Co^{3+}/Co^{2+} at the Co1 site located near Fe^{3+} ions, due to the competition between the crystal field energy and Hund's exchange energy, leading to the distribution of the electrons in the t_{2g} and e_g orbitals [27].

With further decrease of temperature, the ZFC and FC *M-T* curves begin to deviate from the Curie–Weiss line, which may be attributed to the presence of short-range magnetic ordering. A sudden increase in magnetization is evident in the ZFC/FC *M-T* curves for all the samples at low temperatures below T_N, indicating the onset of the long-range AFM order. An additional important magnetic feature of the systems is a separation between the FC and ZFC magnetization starting at a so-called thermal irreversibility temperature T_{irr} along with a cusp at T_f in the ZFC *M-T* curves. These features can be ascribed to the presence of a spin-glass-like magnetic state [45,46], whose nature will be discussed below. Moreover, as the Fe-doping concentration increases, the magnetization shows a monotonous decrease. It indicates the suppression of the FM interchain interaction due to reduced correlation length between the Co2 moments along the *c*-axis. Furthermore, as can be seen in Table 1, the Fe doping causes decrease of T_N, T_{irr}, and T_f, implying the suppression of both the long-range AFM order and the glass-like magnetic phase. The different magnetic characters of Ising Co and Heisenberg Fe spins should thus be responsible for the observed features [27].

To further probe the nature of the low-temperature spin-glass-

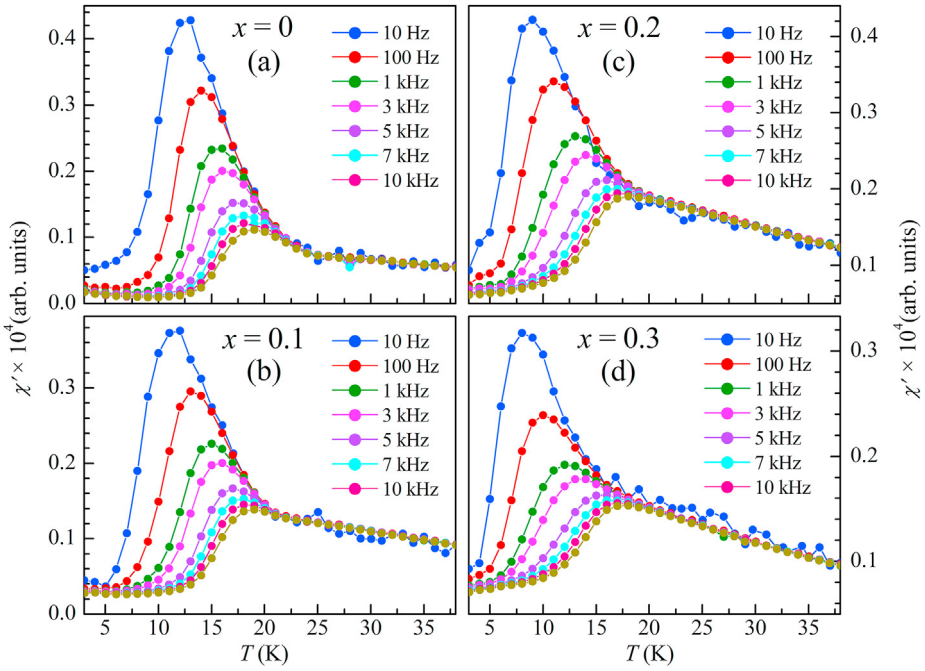

Fig. 6. Temperature dependent *ac* susceptibility measured at an *ac* driving field of 5Oe at selected frequencies for $Ca_3Co_{2-x}Fe_xO_6$ with (a) $x = 0.0$, (b) 0.1, (c) 0.2 and (d) 0.3.

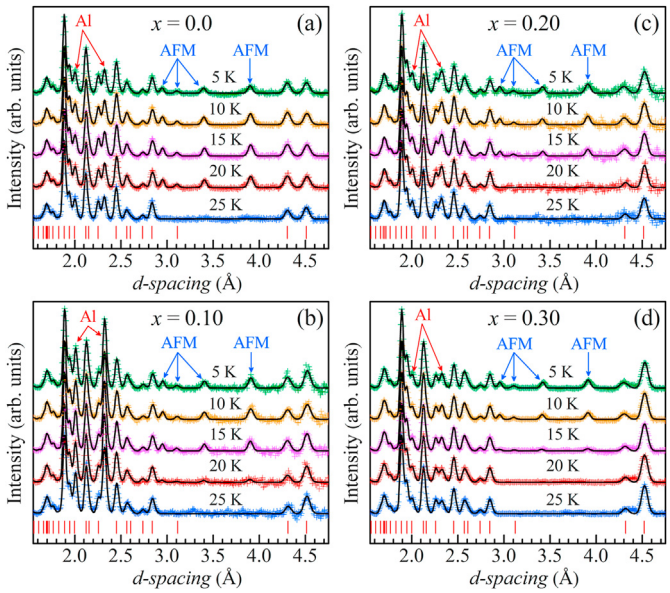

Fig. 8. Low-temperature neutron diffraction patterns of $Ca_3Co_{2-x}Fe_xO_6$ with (a) $x = 0.0$, (b) 0.1, (c) 0.2 and (d) 0.3, refined by the Rietveld method. The experimental points and calculated profiles are shown. The ticks below represent the calculated positions of the nuclear peaks from the structural phase. The most intense peaks of the magnetic phase and Al used as a sample cover are marked by symbols AFM and Al, respectively.

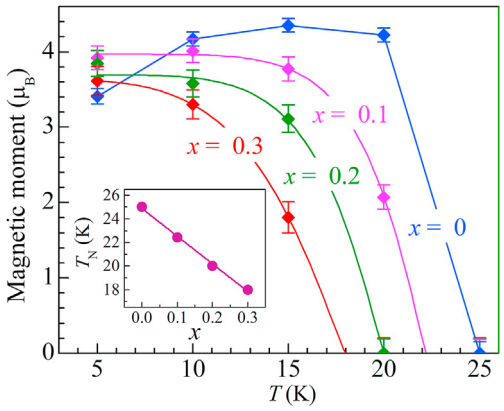

Fig. 9. Temperature dependencies of the average magnetic moment at the Co2 site for $Ca_3Co_{2-x}Fe_xO_6$ and their interpolation by the function $\mu(T) = \mu_0 \cdot (1-(T/T_N)^{\alpha})^{2\beta}$ [55]. The inset shows the concentration dependence of T_N and its linear fit.

like magnetic state, *ac* susceptibility measurements were performed with various frequencies ranging from 10 Hz to 10 kHz at an *ac* driving field of 5 Oe, and the results are present in Fig. 6. For all the samples, broad peaks were observed around the freezing temperature T_f in the $\chi'(T)$ curves, exhibiting a strong frequency dependence. As frequency increases, these peaks exhibit a shift toward to higher temperature and a decrease in intensity (see Fig. 6), reflecting the slow dynamics of $Ca_3Co_{2-x}Fe_xO_6$ compounds, which is typically observed for spin-glass-like systems. The phenomenological parameters, estimated from the frequency-dependent shift of T_f, $K = \Delta T_f/T_f \, \Delta \log f$ [47,48], are 0.143, 0.168, 0.236, 0.252 for $x = 0$, 0.1, 0.2, and 0.3, respectively. For the undoped sample ($x = 0$), the obtained value of K is consistent with that reported previously [16,49]. Notably, these values of K are much larger compared to conventional spin glasses [47,48] but similar to those of superparamagnetic systems [48,50,51]. Such large frequency dependence of *ac* χ' was also been observed in other isostructural spin-chain compounds Ca_3CoIrO_6 [52] and Ca_3CoRhO_6 [53].

As shown in Fig. 7, at 10 K the $M(H)$ curves show two distinct plateaus and steps at quite low field $H_1 \approx 0$ and H_2 above 3.2 T. Additionally, the magnetization (M) on the low-H plateau is equal to 1/3 of that on the high-H one. It has been suggested that the first step of M corresponds to a formation of the ferrimagnetic state with two spins-up and one spin-down ferromagnetic chains on a triangle, while the second one corresponds to its transformation to the full ferromagnetic ordering of the FM chains [27]. By examining the derivative dM/dH, we have found two additional steps at 1.2 and 2.4 T (see inset (b) of Fig. 7). The magnetization multisteps are metastable and suggested to arise from quantum tunneling of the magnetization [49,54]. Upon Fe doping, both the plateaus became smeared out and demonstrated a decrease in their magnetization. Moreover, the value of H_2 decreased continuously as the Fe doping concentration increased (see inset of Fig. 7). These features indicate that the Fe substitution suppressed the intrachain couplings in these samples. One important feature of the $M(H)$ data is the presence of a small hysteresis. It is clearly seen in the inset of Fig. 7a that both remanent magnetization and coercive field decreased with increasing Fe concentration, which is consistent with the reduction of the interchain interactions upon Fe doping as revealed by the *dc* magnetization study.

To probe the evolution of the long-range magnetic order upon Fe doping, we have collected NPD patterns for the samples at low temperatures down to 5 K, and the results are presented in Fig. 8. We have found that for all samples studied, the initial crystal structure symmetry remains unchanged in the whole investigated temperature range (5–300 K). The extra peaks of magnetic nature located at d_{hkl} positions of 3.10, 3.41 and 3.90 Å appeared at low temperatures (Fig. 8). The data analysis has shown that these peaks correspond to the presence of the long-range SDW order. It is important to note that during the magnetic refinements for the samples, the magnetic moment at Co1 site was refined and was found to be near zero within experimental error, indicating a paramagnetic behavior of the spins located at this site. The temperature dependence of the average magnetic moment at the Co2 site of the samples is presented in Fig. 9.

Unlike in the Fe-doped samples, the undoped sample ($Ca_3Co_2O_6$) demonstrates an unusual decrease of the average magnetic moment of Co2 ions below $T = 15$ K, which can be attributed to the development of the short-range magnetic orders as reported earlier [18,19,22]. As can be seen in the inset of Fig. 9, the T_N value shows a linear decrease with increasing Fe-doping level from 25 K for $x = 0$–18 K for $x = 0.3$. Simultaneously, the ordered Co2 magnetic moment value at 5 K decreases nearly linearly from ~3.9 to ~3.6 μ_B as x increases from 0.1 to 0.3, which can be attributed to the magnetic disorder in the Co sublattice, caused by the Fe doping [56]. The trend of T_N and the average magnetic moment are consistent with the observed *dc* magnetization results, confirming the reduction of both intrachain and interchain interactions with Fe doping. On the other hand, the strength of the magnetic interactions is dependent on relevant interatomic distances and bond angles. Thus, a detailed analysis of the Fe-doping dependence of the related structural parameters has been made, and the results are shown in Fig. 10. The refined structural parameters, characteristic bond distances and angles at 30 K are also summarized in Table 2.

According to a previous study [22], the strength of the intrachain FM interactions is determined by the transfer integral between the Co2(HS) and Co1(LS) ions, $J_1 \sim t_{dd}^4 \sim (d_{Co1\text{-}Co2})^{-20}$, while the strength of the interchain AFM interactions is determined by the transfer integrals between the Co2(HS)–O ions and O–O ions, $J_{2,3} \sim t_{pd}^4 t_{pp}^2 \sim (d_{Co2\text{-}O})^{-14} \cdot (d_{O\text{-}O})^{-4}$. As summarized in Table 2, the

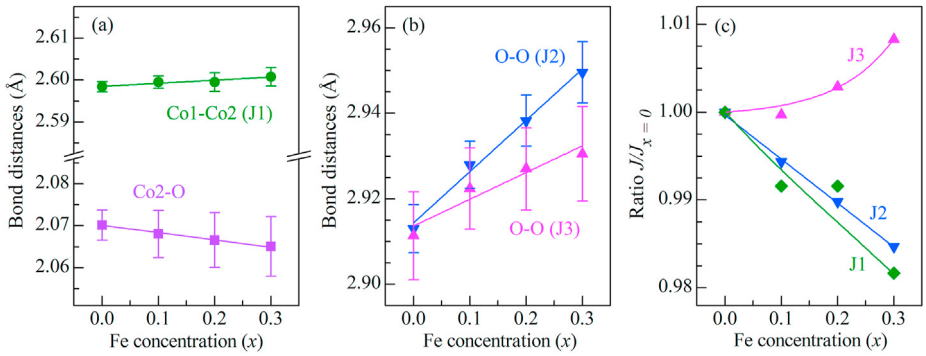

Fig. 10. Fe-concentration dependences of Co1—Co2, Co2—O (a), O—O (b) interatomic distances, and the ratio of strength of magnetic interactions J normalized to its value at $x = 0$ (c).

Table 2
Refined structural parameters, characteristic bond lengths and angles of the $Ca_3Co_{2-x}Fe_xO_6$ systems at 30 K. In the structure of *R-3c* symmetry, atomic crystallographic sites are Ca *18e* (x, 0, 1/4), Co1 *6e* (0, 0, 0), Co2 (Co/Fe) *6a* (0, 0, 1/4), and O *36f* (x, y, z).

x (Fe)	0	0.1	0.2	0.3
a (Å)	9.080 (5)	9.089 (6)	9.092 (6)	9.098 (6)
c (Å)	10.394 (5)	10.398 (6)	10.398 (9)	10.403 (9)
Ca: z	0.3695 (5)	0.3701 (4)	0.3721 (5)	0.3714 (5)
O2: x	0.1781 (5)	0.1772 (5)	0.1766 (5)	0.1760 (7)
y	0.0253 (8)	0.0250 (7)	0.0247 (7)	0.0242 (7)
z	0.1143 (3)	0.1141 (4)	0.1139 (6)	0.1139 (7)
Co1—Co2	2.5985 (12)	2.5995 (15)	2.5995 (22)	2.6007 (22)
Co1—O	1.9256 (64)	1.9202 (43)	1.9159 (67)	1.9141 (58)
Co2—O	2.0702 (36)	2.0680 (56)	2.0666 (67)	2.0651 (71)
O—O (J2)	2.9130 (56)	2.9280 (55)	2.9383 (61)	2.9496 (72)
Co2—O—O (J2)	101.61 (24)	101.58 (23)	101.50 (23)	101.46 (24)
O—O (J3)	2.911 (10)	2.9224 (95)	2.9270 (96)	2.931 (11)
Co2—O—O (J3)	135.78 (23)	135.63 (25)	135.53 (27)	135.58 (34)

values of the interatomic Co2—O—O angles, corresponding to the J2 and J3 interactions, slightly change with varying the Fe-doping concentration and their contribution to the modification of magnetic interactions can be neglected. Based on the experimental values of the structural parameters, the Fe-concentration dependence of the strength of the magnetic interactions normalized to the value at $x = 0$ has been calculated and presented in Fig. 10c. As can be seen in Fig. 10, with increasing x, the distance Co1—Co2 slightly increases, weakening the intrachain interaction J_1. In the case of $J_{2,3}$, a decrease in the Co2—O distance is compensated by a strong increase of the relevant O—O distances. Upon increasing x, J_2 and J_3 show opposite behaviors, e. g. J_2 is weakened in contrast to a weak enhancement of J_3. As a result, the average strength of the interchain interactions slightly decreases.

If taking $J_1 = 23.9$ K, $J_2 = -1.1$ K and $J_3 = -1.2$ K reported for $Ca_3Co_2O_6$ [12] and using the experimental Fe-concentration dependences of their normalized values (Fig. 10c), their absolute values can be calculated. Based on the obtained values of the magnetic interaction strength, the T_N temperature of the long-range SDW order of the studied samples has been estimated using the analytical solutions for the static susceptibility of the one-dimensional Ising model within the mean field approach:

$$\chi(T) = (1 / k_B T)\frac{1}{\cosh\left(\frac{2J_1}{k_B T}\right)}\frac{1}{1-\tanh\left(\frac{2J_1}{k_B T}\right)}, \quad (1)$$

$$\chi^{-1}(T_N) = -2(J_2+J_3). \quad (2)$$

Although this calculation qualitatively reproduces a trend towards T_N reduction upon Fe doping, the evaluated change from 27.0 K for $x = 0$—26.66 K for $x = 0.3$ is significantly less than experimentally observed one (see the inset of Fig. 9). This can be explained due to the Fe-doping induced magnetic disorder and distinct magnetic features of Ising Co and Heisenberg Fe spins, providing additional source for more rapid T_N decrease found in $Ca_3Co_{2-x}Fe_xO_6$.

4. Conclusion

The Fe-doping effects on the structural and magnetic properties of $Ca_3Co_{2-x}Fe_xO_6$ ($x = 0$, 0.1, 0.2 and 0.3) have been systematically investigated. The initial rhombohedral crystal structure remains stable upon Fe doping in the whole temperature range of 10—300 K. The Fe ions locate at the trigonal prism Co2 sites. The Fe doping converts some of the low-spin Co^{3+} ions at the Co1 octahedral sites into Co^{2+} ions, whose fraction remarkably increases with the increase of x. For the high-temperature paramagnetic phase, the sign of the Curie paramagnetic temperature θ_p changes from positive to negative at $x = 0.2$, signalizing the weakening of the FM interactions and the dominance of the AFM interactions at higher Fe concentrations. A partial low-spin to high-spin state crossover of the Co1 ions is observed at the high Fe-doping level ($x = 0.3$). All the samples exhibit a long-range spin-density wave (SDW) AFM ordering, followed by a spin-glass-like transition at lower temperature. The low-temperature magnetic phases are suppressed by the Fe doping. The Fe substitution for Co in $Ca_3Co_{2-x}Fe_xO_6$ weakens both the intrachain and interchain magnetic interactions, caused by the enhanced magnetic disorder due to the different magnetic characters of Ising Co and Heisenberg Fe spins.

CRediT authorship contribution statement

R. Das: Conceptualization, Methodology, Investigation, Formal analysis, Writing - original draft. **N.T. Dang:** Conceptualization, Methodology, Investigation, Formal analysis, Writing - original draft. **V. Kalappattil:** Investigation, Writing - review & editing. **R.P. Madhogaria:** Investigation, Writing - review & editing. **D.P. Kozlenko:** Writing - review & editing. **S.E. Kichanov:** Investigation. **E.V. Lukin:** Investigation. **A.V. Rutkaukas:** Investigation. **T.P.T. Nguyen:** Formal analysis, Writing - review & editing. **L.T.P. Thao:** Formal analysis, Writing - review & editing. **N.S. Bingham:** Investigation, Writing - review & editing. **H. Srikanth:** Supervision, Project administration. **M.H. Phan:** Supervision, Writing - review & editing.

Declaration of competing interest

The authors declare that they have no known competing financial interests or personal relationships that could have appeared to influence the work reported in this paper.

Acknowledgements

Work at USF was supported by the U.S. Department of Energy, Office of Basic Energy Sciences, Division of Materials Sciences and Engineering under Award No. DE-FG02-07ER46438 (Sample synthesis and magnetic studies). This work was also supported by the Vietnam National Foundation for Science and Technology Development (NAFOSTED) under grant number 103.02-2017.364 and the Russian Foundation for Basic Research, Grant No. 18-02-00359-a (XRD and ND studies).

References

[1] M. Kenzelmann, A.B. Harris, S. Jonas, C. Broholm, J. Schefer, S.B. Kim, C.L. Zhang, S.-W. Cheong, O.P. Vajk, J.W. Lynn, Phys. Rev. Lett. 95 (2005), 087206.
[2] J. Van Den Brink, D.I. Khomskii, J. Phys. Condens. Matter 20 (2008) 434217.
[3] V. Kiryukhin, S. Lee, W. Ratcliff, Q. Huang, H.T. Yi, Y.J. Choi, S.W. Cheong, Phys. Rev. Lett. 102 (2009) 187202.
[4] P.L. Li, X.Y. Yao, K.F. Wang, C.L. Lu, F. Gao, J.M. Liu, J. Appl. Phys. 104 (2008), 054111.
[5] Y.J. Choi, H.T. Yi, S. Lee, Q. Huang, V. Kiryukhin, S.W. Cheong, Phys. Rev. Lett. 100 (2008), 047601.
[6] S.D. Kaushik, S. Rayaprol, J. Saha, N. Mohapatra, V. Siruguri, P.D. Babu, S. Patnaik, E.V. Sampathkumaran, J. Appl. Phys. 108 (2010), 084106.
[7] P. Ding, L. Li, Y.J. Guo, Q.Y. He, X.S. Gao, J.M. Liu, Appl. Phys. Lett. 97 (2010) 2010.
[8] T. Basu, K.K. Iyer, K. Singh, E.V. Sampathkumaran, Sci. Rep. 3 (2013) 3104.
[9] L. Lin, Y.L. Xie, M.F. Liu, Y.J. Guo, Z.B. Yan, J.M. Liu, J. Appl. Phys. 114 (2013).
[10] P. Lampen, N.S. Bingham, M.H. Phan, H. Srikanth, H.T. Yi, S.W. Cheong, Phys. Rev. B 89 (2014) 144414.
[11] E.V. Sampathkumaran, N. Fujiwara, S. Rayaprol, P.K. Madhu, Y. Uwatoko, Phys. Rev. B 70 (2004), 014437.
[12] G. Allodi, P. Santini, S. Carretta, S. Agrestini, C. Mazzoli, A. Bombardi, M.R. Lees, R. De Renzi, Phys. Rev. B 89 (2014) 104401.
[13] Y. Kamiya, C.D. Batista, Phys. Rev. Lett. 109 (2012), 067204.
[14] R. Frésard, C. Laschinger, T. Kopp, V. Eyert, Phys. Rev. B 69 (2004) 140405.
[15] N. Bellido, C. Simon, A. Maignan, Phys. Rev. B 77 (2008), 054430.
[16] A. Maignan, C. Michel, A.C. Masset, C. Martin, B. Raveau, Eur. Phys. J. B 15 (2000) 657.
[17] V. Hardy, S. Lambert, R. Lees, D. McK. Paul, Phys. Rev. B 68 (2003), 014424.
[18] S. Agrestini, L.C. Chapon, A. Daoud-Aladine, J. Schefer, A. Gukasov, C. Mazzoli, M.R. Lees, O.A. Petrenko, Phys. Rev. Lett. 101 (2008), 097207.
[19] S. Agrestini, C.L. Fleck, L.C. Chapon, C. Mazzoli, A. Bombardi, M.R. Lees, O.A. Petrenko, Phys. Rev. Lett. 106 (2011) 197204.
[20] T. Ishikawa, J. Phys. Soc. Japan 52 (1983) 1774.
[21] M. Mekata, J. Phys. Soc. Japan 42 (1977) 76.
[22] D.P. Kozlenko, N.T. Dang, N.O. Golosova, S.E. Kichanov, E.V. Lukin, P.J. Lampen Kelley, E.M. Clements, K.V. Glazyrin, S.H. Jabarov, T.L. Phan, B.N. Savenko, H. Srikanth, M.H. Phan, Phys. Rev. B 98 (2018) 134435.
[23] H. Kageyama, K. Yoshimura, K. Kosuge, X. Xu, S. Kawano, J. Phys. Soc. Japan 67 (1998) 357.
[24] A. Jain, S.M. Yusuf, S.S. Meena, C. Ritter, Phys. Rev. B 87 (2013) 1.
[25] I. Nowik, A. Jain, S.M. Yusuf, J.V. Yakhmi, Phys. Rev. B 77 (2008), 054403.
[26] L.C. Chapon, Phys. Rev. B 80 (2009) 172405.
[27] A. Jain, S. Singh, S.M. Yusuf, Phys. Rev. B 74 (2006) 174419.
[28] H. Kageyama, K. Yoshimura, K. Kosuge, H. Nojiri, K. Owari, M. Motokawa, Phys. Rev. B 58 (1998) 11150.
[29] A. Jain, S.M. Yusuf, J. Campo, L. Keller, Phys. Rev. B 79 (2009) 184428.
[30] D. Kozlenko, S. Kichanov, E. Lukin, B. Savenko, Crystals 8 (2018) 331.
[31] J. Rodríguez-Carvajal, Phys. B 192 (1993) 55.
[32] N. Fairley, A. Carrick, The Casa Cookbook, Acolyte Science, Cheshire, U.K., 2005.
[33] R.P. Madhogaria, R. Das, E.M. Clements, V. Kalappattil, M.H. Phan, H. Srikanth, N.T. Dang, D.P. Kozlenko, N.S. Bingham, Phys. Rev. B 99 (2019) 104436.
[34] J. Song, B. Zhao, Y. Huang, Y. Qin, W. Song, Y. Sun, J. Am. Ceram. Soc. 100 (2017) 3589.
[35] J. Song, B. Zhao, Y. Huang, Y. Qin, J. Zhou, W. Song, Y. Sun, RSC Adv. 7 (2017) 2745.
[36] J.Y. Song, B.C. Zhao, Y.N. Huang, Y.F. Qin, J.F. Zhou, W.H. Song, Y.P. Sun, J. Alloys Compd. 695 (2017) 2506.
[37] P. Woodward, D. Cox, E. Moshopoulou, Phys. Rev. B 62 (2000) 844.
[38] H. Kawanaka, E. Kawawa, Y. Nishihara, F. Iga, A. Kondo, K. Kindo, Y. Matsuda, AIP Adv. 8 (2018) 4.
[39] Y. Takeda, S. Naka, M. Takano, T. Shinjo, T. Takada, M. Shimada, Mater. Res. Bull. 13 (1978) 61.
[40] A. Tkach, P.M. Vilarinho, A.L. Kholkin, Acta Mater. 53 (2005) 5061.
[41] R.D. Shannon, Acta Crystallogr. Sect. A 32 (1976) 751.
[42] T. Burnus, Z. Hu, M.W. Haverkort, J.C. Cezar, D. Flahaut, V. Hardy, A. Maignan, N.B. Brookes, A. Tanaka, H.H. Hsieh, H.J. Lin, C.T. Chen, L.H. Tjeng, Phys. Rev. B 74 (2006) 245111.
[43] X.X. Wang, J.J. Li, Y.G. Shi, Y. Tsujimoto, Y.F. Guo, S.B. Zhang, Y. Matsushita, M. Tanaka, Y. Katsuya, K. Kobayashi, K. Yamaura, E. Takayama-Muromachi, Phys. Rev. B 83 (2011) 100410.
[44] H. Wu, M.W. Haverkort, Z. Hu, D.I. Khomskii, L.H. Tjeng, Phys. Rev. Lett. 95 (2005) 186401.
[45] J. Song, B. Zhao, Y. Huang, Y. Qin, W. Song, Y. Sun, Curr. Appl. Phys. 17 (2017) 738.
[46] J.Y. Song, B.C. Zhao, Y.N. Huang, Y.F. Qin, X.B. Zhu, W.H. Song, Y.P. Sun, Ceram. Int. 42 (2016) 8955.
[47] M. Mezard, G. Parisi, M.A. Virasoro, D.J. Thouless, Spin Glass Theory and beyond, World Scientific, Singapore, 1988.
[48] J.A. Mydosh, Spin-Glasses: an Experimental Introduction, Taylor and Francis, London, 1993.
[49] V. Hardy, D. Flahaut, M.R. Lees, O.A. Petrenko, Phys. Rev. B 70 (2004) 214439.
[50] J.L. Dormann, D. Fiorani, E. Tronc, J. Magn. Magn. Mater. 202 (1999) 251.
[51] V.K. Anand, D.T. Adroja, A.D. Hillier, Phys. Rev. B 85 (2012), 014418.
[52] S. Rayaprol, K. Sengupta, E.V. Sampathkumaran, Phys. Rev. B 67 (2003) 180404.
[53] E.V. Sampathkumaran, A. Niazi, Phys. Rev. B 65 (2002) 180401.
[54] V. Hardy, M.R. Lees, O.A. Petrenko, D.M. Paul, D. Flahaut, S. Hébert, A. Maignan, Phys. Rev. B 70 (2004), 064424.
[55] V.Y. Pomjakushin, A.M. Balagurov, T.V. Elzhov, D.V. Sheptyakov, P. Fischer, D.I. Khomskii, V.Y. Yushankhai, A.M. Abakumov, M.G. Rozova, E.V. Antipov, M.V. Lobanov, S.J.L. Billinge, Phys. Rev. B 66 (2002) 184412.
[56] D.P. Kozlenko, N.T. Dang, T.L. Phan, S.E. Kichanov, L.H. Khiem, S.G. Jabarov, T.A. Tran, T.V. Manh, A.T. Le, T.K. Nguyen, B.N. Savenko, J. Alloys Compd. 695 (2017) 2539.